Cite this: *J. Anal. At. Spectrom.*, 2011, **26**, 1183

www.rsc.org/jaas

PAPER

Kinetic energy and spatial distribution of ions in high irradiance laser ionization source

Yiming Lin,[a] Ruibin Xu,[a] Lingfeng Li,[a] Wei Hang,*[ab] Jian He[c] and Benli Huang[a]

Received 4th January 2011, Accepted 8th February 2011
DOI: 10.1039/c1ja00002k

Characteristics of laser ionization in vacuum and low pressure background gas (He) have been investigated through the measurement of kinetic energy and spatial distributions of copper and tungsten ions. A Q-switched Nd:YAG laser with 532 nm wavelength was utilized and the laser irradiance was fixed at 9×10^9 W cm^{-2}. A plume splitting was observed in the low pressure regime investigated (from 100 Pa to 2000 Pa). The plume propagation translates from a free expansion in vacuum to shockwave-like expansion at relative low pressure and finally diffusion into background gas at relative high pressure environment. A measurement of ion spatial distribution in the ion source has also been carried out for characterizing ions at different pressures and the behaviors of doubly charged, singly charged, and polyatomic ions to reveal the effect of plume–background gas interaction.

1. Introduction

Laser ablation and ionization have received a great deal of attention and comprise a growing area of research due to their importance in thin film deposition,[1] cluster production,[2] nanoparticle formation and growth,[3] as well as general solid analysis.[4–6] Its mechanisms, including target melting, vaporization, plasma formation and expansion, have been studied extensively. The processes of plume expansion into an ambient gas are rather complicated and elusive. The background gas species and their pressures are thought to be important, as they participate in and complicate the plume propagation considerably compared to the expansion in high vacuum, which leads to some dramatic effects, *e.g.* scattering and cooling of ions, plume confinement and splitting effect, formation of shockwaves, and recombination processes, *etc.*[7] Despite the extensive study reported in the literature, expansion dynamics of laser-produced plasma remains an incompletely understood subject. In a low pressure source, the plume splitting characterized by a fast and slow component is usually investigated through spectroscopic studies or modeling methods. Harilal *et al.* made a series of researches on the plume splitting through an intensified CCD camera and found that the phenomenon can only be observed in a particular pressure (4∼40 Pa of Ar) and distance (>4 mm) range.[8–10] The distance-related pressure dependency was also observed by Amoruso *et al.*[11,12] A model combining multiple elastic scattering and hydrodynamic formulation was proposed by Wood *et al.* to give a coherent explanation of the observed splitting of the plume into twin peak distribution.[13,14]

Optical spectroscopic studies are suited for characterizing neutral and excited species, which reveal only a part of ablated species. The line emissions from the multiply charged ions occur close to the target surface, which are difficult to be observed due to the continuum emission from hot plasma at the time of plasma initiation. Moreover, the emissive properties of excited multiply charged ions lie in the vacuum ultraviolet (VUV) or even the soft X-ray range. Practical application of LIBS is complicated due to the lack of gated (iCCD) detector with adequate sensitivity and the requirement of non-VUV-absorbing optics.[15–17] It is even hard for the spectroscopic technique to acquire the information of polyatomic ions together with atomic information. In contrast to optical spectroscopic diagnostic techniques, mass spectrometry allows for the investigation of charged species (singly charged, multiply charged, and polyatomic ions) in the plume and provides useful information about the ion yields of the ablated particles. The analysis of charged species is paramount for understanding both the elementary and the macroscopic processes involved in laser ablation and ionization, especially when a background gas is present.[18] Most meaningful studies using mass-spectrometric analysis have focused on the angular and velocity distributions of the emitted ions. In particular, TOFMS allows the simultaneous identification of all ionized species through their *m*/*z* values and is capable of analyzing the energies of the species from each laser shot.

In this paper, the kinetic energies of the ions are investigated through the temporal distribution made by varying the deflect voltage in the TOF analyzer and the delay time between the laser shot and the repelling pulse. The relationship of the kinetic energy and deflect voltage is simulated by SIMION. A plume

[a]*Department of Chemistry, Key Laboratory of Analytical Sciences, College of Chemistry and Chemical Engineering, Xiamen University, Xiamen 361005, China. E-mail: weihang@xmu.edu.cn*
[b]*State Key Laboratory of Marine Environmental Science, Xiamen University, Xiamen 361005, China*
[c]*Department of Mechanical and Electrical Engineering, Xiamen University, Xiamen 361005, China*

splitting was observed in the pressure regime tested. The topological graphs showing the spatial distributions of specific ions in the ion source are also obtained to reveal the expansion dynamics of the doubly charged, singly charged, and polyatomic ions. The results reveal the effects of strong plume–background gas interaction in the buffer-gas-assisted source.

2. Experimental setup

An in-house-built laser ionization orthogonal time-of-flight mass spectrometer (LI-*O*-TOFMS) that had been described previously was used in the experiment.[19,20] A simple schematic diagram of the experimental apparatus is shown in Fig. 1. A Q-switched Nd:YAG laser (Dawa100, Beamtech Inc., China) with a pulse width of 5 ns and a wavelength of 532 nm was utilized. The laser beam was focused onto the sample surface by a single quartz lens with a focal spot diameter of 50 μm. Two sets of electrical static lenses and a set of direct-current quadrupoles (DCQ) were employed for ion transmission. Steering plates were used inside the flight tube to adjust the trajectory of the ions. The output signal from micro-channel plates (MCP) was registered on a digital storage oscilloscope (42Xs, Lecroy, USA) for spectrum acquisition. The integrated ion intensity was the accumulation of 80 mass spectra induced by 80 laser pulses. Typical operating parameters are listed in Table 1.

Target disks (6 mm in diameter, 1.5 mm thickness) made of copper (99.9% purity) or tungsten (99.0% purity) were immobilized by Kapton tape on top of the direct insertion probe (DIP). Ultra-high purity helium (99.999%) was used as the background gas; and the gas flow was controlled by a needle valve.

3. Result and discussion

Our instrument is capable of measuring the temporal distributions of the ionic species by varying the delay times between the laser shots and the repelling pulses.[21] When the ionic species went through the nozzle and ion optics, they can form a beam-shaped ion packet, which means that the ions in different locations of the ion packet will reach the repelling region in different times (Fig. 1). By varying the delay time between the laser pulse and repelling pulse, the ion intensities of various parts in the ion packet can be measured. The temporal distribution of one species is obtained by the correlating intensities in the mass spectra with different delay times. Another strength lies in that the deflect voltage is a direct indicator of the kinetic energy of ions from the ion source. The repelling region, when no pulse is applied, is at ground potential; thus, ions arriving in this region keep their initial kinetic energy in the *X* direction (Fig. 1) when leaving the source. By changing the deflect voltage, ions of different kinetic energies in the ion packet are detected selectively. With the double characterization (delay time and deflect voltage), results of ion kinetic energies can be obtained under different laser ionization conditions. For example, such measurements were made on a copper target at 600 Pa background gas pressure, and the resulting distributions are shown in Fig. 2. When the deflect voltage is −3000 V, the electric field between the steering plates is so strong that only high kinetic energy ions (at short delay time) can reach the detector, and ions with low kinetic energy (at long delay time) will be completely deflected and cannot be detected. In the mediated voltage (−3500 V), the ions with low kinetic energy begin to emerge. With the deflect voltage growing negative, more and more of the fast component hit the steer plates or inner chamber wall, leaving only the slow component. Through the SIMION simulation, the relationship of the deflect voltage and kinetic energy of ions is shown in Fig. 3. A deflect voltage of −2500 V corresponds to a kinetic energy of 724 eV, and −5000 V corresponds to about 14 eV.

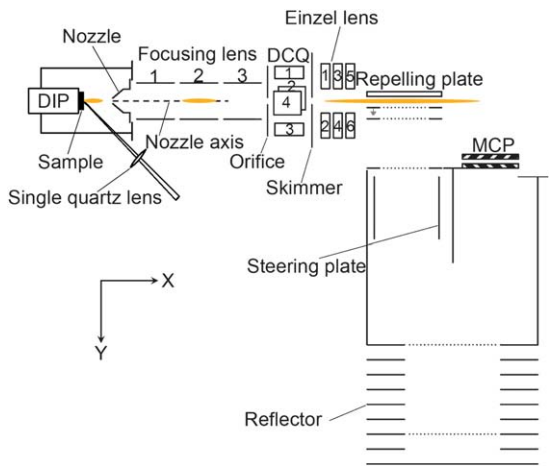

Fig. 1 Schematic diagram of LI-*O*-TOFMS.

Table 1 Typical operating parameters of LI-*O*-TOFMS

Ion source	
Laser pulse frequency	10 Hz
Laser pulse duration	5 ns
Laser wavelength	532 nm
Laser fluence	9×10^9 W cm^{-2}
Laser incident angle	45°
Spot diameter	50 μm
Distance from sample surface to nozzle	10 mm for temporal distribution measurement and 6–14 mm for ion spatial distribution
Source chamber pressure	Vacuum (0.03 Pa) ~ 2000 Pa
Transportation system	
Nozzle	20.0 V
Focusing lens 1 (electrode 1, 2, 3)	−78 V, −54.6 V, −110 V
Orifice	−30 V
DCQ (electrode 1, 2, 3, 4)	−16.7 V, −16.39 V, −6.87 V, −16.28 V
Skimmer	−52.9 V
Einzel lens (electrode 1, 2, 5, 6)	Ground
Einzel lens (electrode 3, 4)	−15.0 V, −16.0 V
TOF mass analyzer	
Repelling frequency	10 Hz
Repelling pulse magnitude	750 V
Repelling pulse duration	2.5 μs
Acceleration potential	−5000 V
Deflect voltage on steering plate	−2500~−5000 V

3.1 Laser ionization in vacuum

It has been reported that ions generated in the nascent erosion plasma expand freely into a vacuum with kinetic energies ranging from several eV to thousands of eV with high laser irradiance (10^9 W cm^{-2} and above).[7,22] The temporal distributions of Cu^+ at

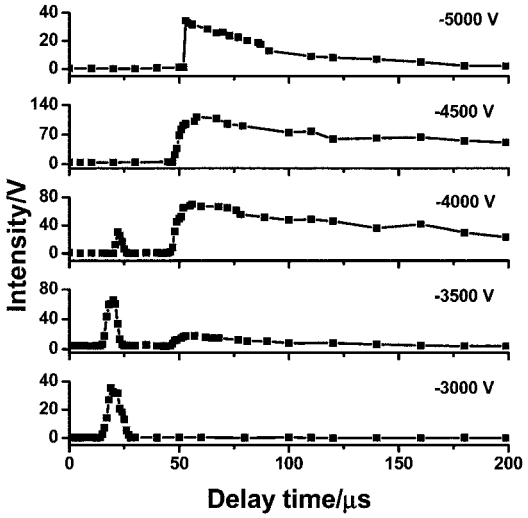

Fig. 2 Temporal distributions of Cu^+ in different deflect voltages at 600 Pa.

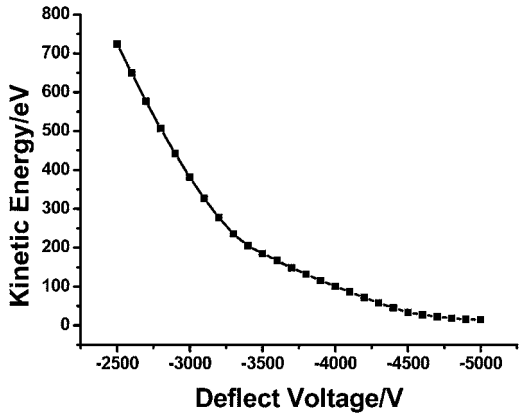

Fig. 3 The relationship between the deflect voltage and ion kinetic energy through SIMION 7.0 simulation.

different deflect voltages are shown in Fig. 4. When the deflect voltage grows negative, the delay time for the maximum intensity (T_{max}) also becomes longer, indicating the lower kinetic energy of the ions been detected. Kinetic energy distributions of ions in individual delay times are plotted in Fig. 5a. Since the delay times have an equal interval, a simple accumulation of the signal profiles (in Fig. 5a) can reasonably represent the overall kinetic energy distribution of ions in a vacuum source (as shown in Fig. 5b). Most of the ions have their kinetic energies of several hundreds of eV, and the most probable value is about 200 eV.

The temporal distributions of Cu^{2+} in different deflect voltages are displayed in Fig. 6. Behaving similarly to that of singly charged ions, the T_{max} of doubly charged ions moves toward the longer delay time with the deflect voltage growing negative. However, T_{max} values of Cu^{2+} at fixed deflect voltages (in Fig. 6) are smaller than those of Cu^+ (in Fig. 4), indicating the higher velocity of doubly charged ions. It is worth stressing that, during laser ablation and ionization, hot electrons are emitted from the target more quickly than the ions, and thus an electrostatic barrier is built near the target. Due to their high charge states,

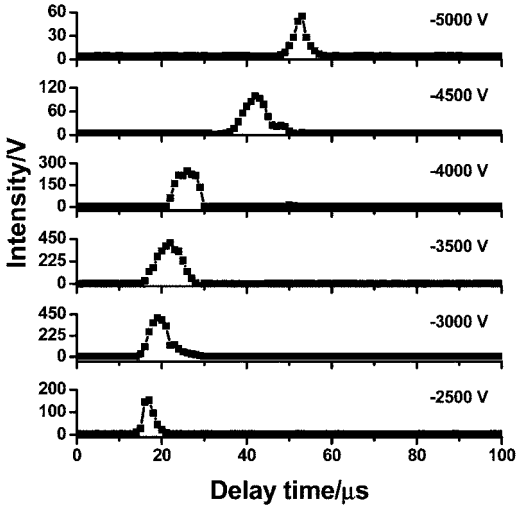

Fig. 4 Temporal distributions of Cu^+ in different deflect voltages in vacuum.

multiply charged ions are accelerated more quickly than singly charged ions,[18] which propels them to the front of the plume. As a consequence, the doubly charged ions in the sheath of the plasma plume acquire more laser energy during hydrodynamic expansion than the singly charged ions, resulting in the higher kinetic energy obtained.[8]

3.2 Laser ablation in low pressure background gas

In an ambient gas, the expansion of the plasma plume can be quite complex. The property and pressure of the background gas have a strong effect on the expansion dynamics of the plume. Helium was chosen as the buffer gas due to the high ionization potential (24.5 eV), and thus the ionization of the background gas can be ignored. The temporal distributions of Cu^+ in different deflect voltages are presented in Fig. 7 with the He pressure ranging from 100 Pa to 2000 Pa. As mentioned above, when the deflect voltage is high (less negative), the electric field between the steering plates is so strong that ions with lower kinetic energy (longer delay time) can be completely deflected, resulting in only the fast component being detected by the MCP. In the mediated deflect voltage, both the fast and slow components can be observed simultaneously. With the deflect voltage growing negative, the fast component in the ion packet disappears due to the hit on the steer plate or wall chamber, leaving only the slow component. A twin peak distribution representing the fast and slow components in the plume was observed in the mediated deflect voltage (−3500∼−4000 V in Fig. 7), indicating the existence of plume splitting. In particular, the plume splitting was commonly observed and discussed by other groups through ion probe, optical emission spectroscopy, or the hydrodynamic model.[9,11,23] A self-consistent ambipolar electric field (so-called double layer) theory was suggested by Bulgakova *et al.* as a possible mechanism responsible for this phenomenon.[24] In vacuum condition, plume propagation is an adiabatic free expansion process. However, in the low pressure regime, plume behavior is characterized by the strong interpenetration of the laser plasma and ambient gas as a consequence of

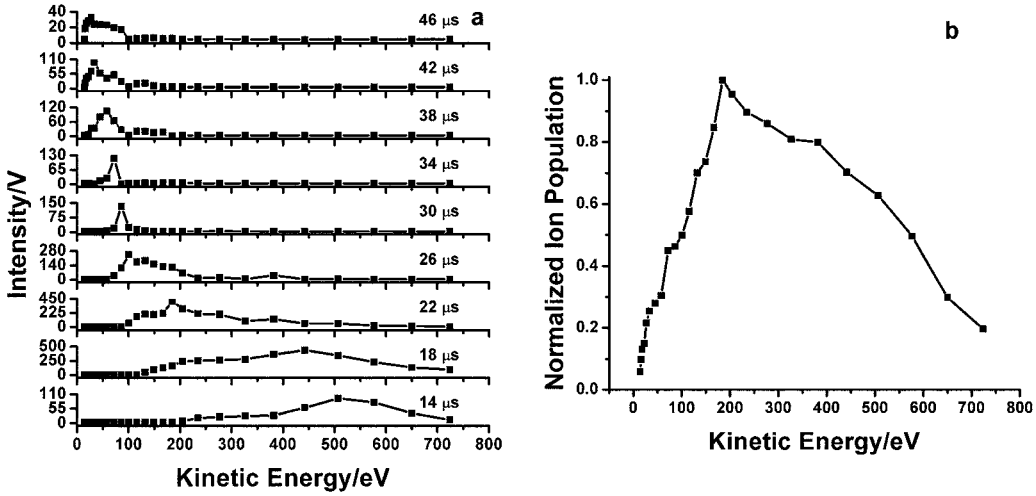

Fig. 5 Kinetic energies of Cu^{+} in (a) individual delay times and (b) overall distribution.

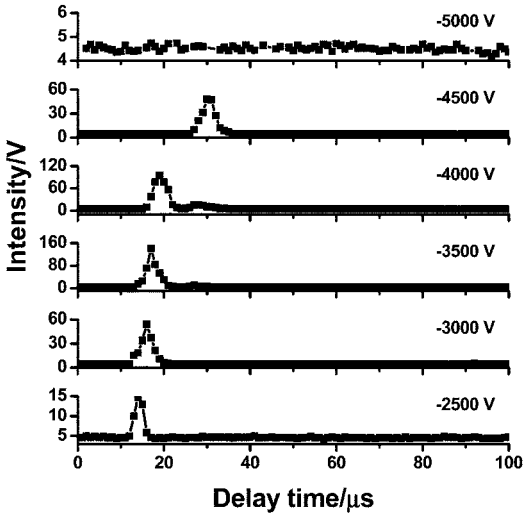

Fig. 6 Temporal distributions of Cu^{2+} in different deflect voltages in vacuum.

plume–background gas interaction. It can be found in Fig. 7 that the plume splitting is characterized by an energetic component that composes only a small part of the ion population and a slow component that contributes the majority of the ionized species at the relative high background pressure.

The fast component shows vacuum-like temporal distributions with the similar T_{max} (~20 μs) which is very close to the vacuum condition (see Fig. 4). During the interpenetration of the laser plasma and ambient gas, fast ions experience almost no collision with the background gas, resulting in the propagation at vacuum velocity and no delay on T_{max} by increasing the pressure. This small group of energetic ions transports a significant fraction of the laser energy absorbed.[10] For the second delayed component, due to the collisions between the plume ions and helium atoms, its kinetic energy is attenuated, and this attenuation becomes more severe with the increase of pressure. Thus, in the following section, we will focus on the slow component, which represents the majority of the ion population in the buffer-gas-assisted source.

From the view of adiabatic expansion, the plume length is estimated according to the expression:[21,25]

$$L_p = A[(\gamma - 1)E]^{1/(3\gamma)} P^{-1(3\gamma)} V^{(\gamma-1)/(3\gamma)} \quad (1)$$

where A is the geometrical expansion factor related to the expansion angle, γ is the ratio of the specific heats of the plume species, E and P are the laser energy (J) and gas pressure (Pa), respectively, and V is the initial volume of laser ablation in m^3. Considering our experimental condition ($A = 1.6$, $\gamma = 1.67$ for monatomic molecules, $V = 1.25 \times 10^{-8}$ m^3), the expression can be shortened to:

$$L_p = 0.13(E/P)^{0.2} \quad (2)$$

The plume length is estimated as about 11.4 mm for 100 Pa, which is longer than the sampling distance (10 mm). Thus the ions are not totally slowed down by the retarding of ambient gas and maintain part of their kinetic energy. When the pressure is 600–2000 Pa, an increasing number of collisions takes place. The plume length is estimated as 6~8 mm in this pressure regime, which is shorter than the sampling distance. Once the ejected species have traversed the plume length, they lose their kinetic energy and their movement changes from a hydrodynamic process to a thermodynamic diffusion process. To further elucidate the underlying mechanism, the apparently different behaviors of the slow component at 100 Pa and 600–2000 Pa of He will be discussed separately.

At the relative low pressure of 100 Pa, the elastic scattering theory can be used to interpret the expansion dynamics. Based on the fact that helium atoms are inert and the speed of ablated species is much larger than that of the He atom at room temperature, the collisions between the ions and He atoms are elastic and He atoms are static relative to the ablated species. Thus the mean free path (MFP) of ions can be calculated as:[26,27]

$$\lambda = \frac{k_B T}{\pi p (d_{He} + d_{Cu})^2} \quad (3)$$

where λ is MFP, p is the gas pressure, T is the background gas temperature, k_B is the Boltzmann constant, d_{He} and d_{Cu} are the

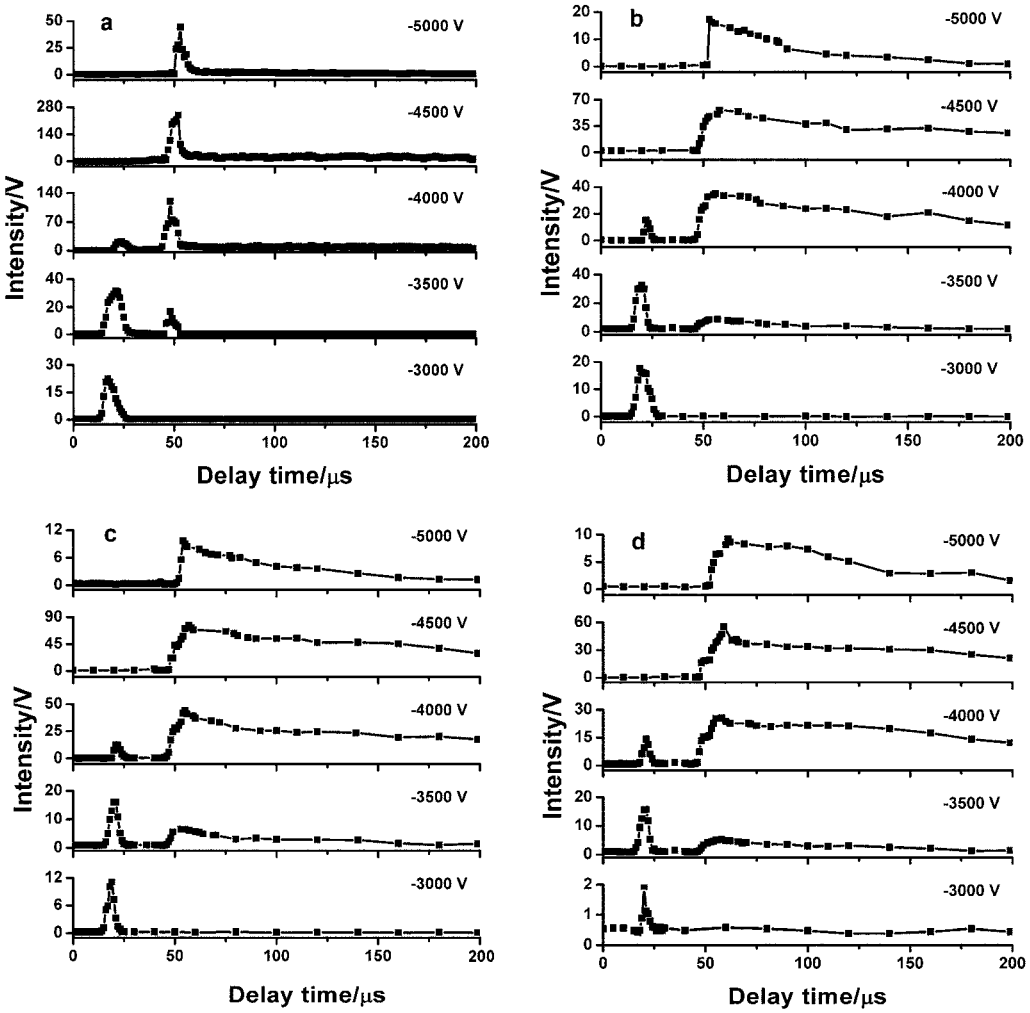

Fig. 7 Temporal distributions of Cu^+ in different deflect voltages at (a) 100 Pa, (b) 600 Pa, (c) 1000 Pa, and (d) 2000 Pa pressure of He.

effective radii of the He atom and Cu^+ respectively. The MFP of Cu^+ is estimated as 0.5 mm at 100 Pa, which is much shorter than the sampling distance (10 mm). Collisions with the background gas atoms begin to play a role. Energy and momentum exchange takes place due to the ion–background gas collisions, ion–ion coulombic scattering, charge exchange interactions, *etc*.[9] The strong plume–background gas interaction leads to the shock-wave generation. The plume goes through a collisional and shockwave-like hydrodynamic expansion. Assuming the elastic scattering condition, the maximum energy loss of Cu^+ in one collision can be estimated as:[28]

$$\frac{\Delta E_{\max}}{E} = \left[4(m_{\mathrm{He}}m_{\mathrm{Cu}})/(m_{\mathrm{He}} + m_{\mathrm{Cu}})^2\right] \quad (4)$$

During a head-on collision with the background gas atom, the maximum energy loss $\Delta E_{\max}$ of Cu^+ is about 20% of its initial kinetic energy. However, in reality, many factors complicate the collision processes. Firstly, most of collisions are non-head-on collisions;[29] secondly, the partial pressure of helium is lower in the center of the plume than that in the surrounding area due to the high plasma temperature; thirdly, the background gas is diluted by the collisions because a fraction of the background gas is driven out of the interaction volume,[30] *etc*. These complications are beyond our ability to illustrate the collision process theoretically, but there is no doubt that the collision will cool the ablated species and the energy loss during one collision is much lower than 20%. The experimental result shown in Fig. 8 indicates that the ambient gas collision significantly reduces the kinetic energy of the ions compared to that in the vacuum condition, not only the narrower of the distribution, but also the

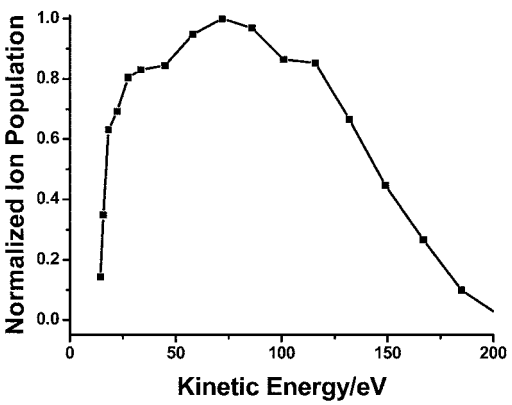

Fig. 8 Kinetic energy distribution of Cu^+ at 100 Pa pressure of He.

lower of the most probable kinetic energy (from ~200 eV in Fig. 5b to ~70 eV in Fig. 8).

As the background gas pressure is further increased to 600–2000 Pa, the plume length will be shorter than the target–nozzle distance, as illustrated previously. The MFP in this pressure regime is estimated as 0.025~0.08 mm. The collision number for the target–nozzle distance increases as high as 125 even at 600 Pa. Thus, most of the ablated species are slowed down and thermalized after so many collisions. The broad distributions of the slow component (in Fig. 7b, c, and d) result from the complicated processes in the ion source and are further exacerbated by the ion optics. Before the plume expands to its plume length, there exists elastic scattering between the ablated species and the ambient gas atom. Through the transfer of energy to the background gas, the ablated species lose their initial kinetic energies and depart from their initial trajectories. After the slow ions reached the plume length and lost their kinetic energies, they move randomly in a thermodynamic diffusion process from L_p to the nozzle, and confuse with the background gas, which leads to the broad temporal distribution of the slow component. Most of the ions being sampled into nozzle are thermalized with kinetic energy equivalent to the thermal energy at the ion source. Thus, all slow components in this pressure regime show similar T_{max} values in the temporal distribution, regardless of the background gas pressure. This result is coincident with the kinetic energy distributions presented in Fig. 9, where the ions exhibit similar kinetic energy distributions with the most probable value at ~33 eV at the pressure of 600–2000 Pa, indicating the same thermal diffusion motion. The 33 eV value could be the combination of the 20 V nozzle potential (the target was floated) and the plasma potential (*e.g.* 13.8 eV obtained by Dreyfus in 10^9 W cm^{-2} laser irradiance for a Cu target[31]). Comparing with the case in relative low pressure of 100 Pa (Fig. 8), the energy of thermalized ions is much lower than that of the hydrodynamic controlled ions (33 eV *vs.* 70 eV).

In summary, the plume expands freely in a vacuum condition. As the ambient gas pressure increases, the plume behavior is characterized by strong plume–background gas interaction. There are different stages which involve the plume confinement, splitting, shockwave formation, plume–background gas mixing, *etc*. In the pressure regime investigated, there exits a plume splitting which is characterized by a fast component at vacuum-like velocity and a slow component determined by the background gas pressure. At the relative low pressure of 100 Pa, plume–background gas collisions lead to the shockwave generation. At even higher gas pressure (600–2000 Pa), thermalization was observed with the ablated species tending to diffuse out of the plume into the background gas. To further characterize the plume dynamic, the topological graphs illustrating ion spatial distributions in the ion source were also made, which will be discussed in the following section.

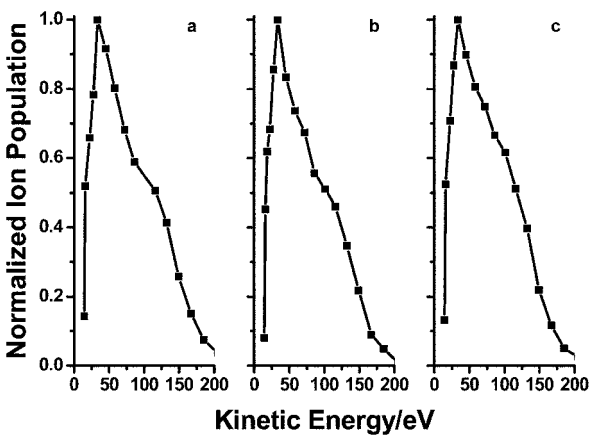

Fig. 9 Kinetic energy distributions of Cu^+ at (a) 600 Pa, (b) 1000 Pa, and (c) 2000 Pa pressure of He.

3.3 Ion spatial distribution in vacuum and low pressure background gas

The formation of non-isotropic plasma plume caused by the collisional processes in the Knudsen layer results in a strong forward-peaked expansion of the ablated species with a maximum emission according to the target normal.[32] The angular distribution of emitted species can be described by a $\cos^n\theta$ distribution based on a free jet expansion theory, where n is the sharpness parameter.[33,34] If the ablated material expands into the background gas, the angular distributions are extremely sensitive to the properties and pressure of the ambient gas.[35,36] By moving the DIP in the X direction and the laser spot in the Y direction (Fig. 1), our instrument is capable of acquiring of the spatial distribution of ions.

In order to include the polyatomic ions in the study, tungsten was chosen because of the easy formation of WO^+. Typical topological graphs of W^+ in vacuum and relative low and high pressures are shown in Fig. 10. The topological graphs were made by the software Surfer V9. One dimension represents the laser spot position; the second dimension represents the nozzle–sample distance. In all conditions, it is a forward-peaked expansion with the highest intensity according to the target normal. In vacuum without any ambient gas, the deflect voltage was set at −3500 V to acquire the maximum intensity. Ions generated in the nascent erosion plasma expand freely. The ion intensity grows up with the sample–nozzle distance and shows the maximal value at the largest target–nozzle distance for the mechanic limitation of our instrument (Fig. 10a). The plume is highly forward with ion current decreases sharply away from the nozzle axis. In an ambient gas environment, the expansion of the plume is quite complicated. Multiple collisions will take place, which reduces the kinetic energy of the ions (thus, the deflect voltage was set at −4200 V at 100 Pa and −4500 V at 600 Pa for the maximum slow component) and results in broad angular distributions (Fig. 10b and c). Compared with the vacuum condition, the decrease of ion current from the nozzle axis is much more gradual, indicating the broadening effect of background gas through increasing collisions. Moreover, the plume is prolonged along the target normal and suppressed in the direction parallel to the target surface during the expansion. From Fig. 10, it can be found that, due to the confinement of background gas, the distribution of W^+ in the plume changes with the location of maximal ion intensity from 14 mm in the vacuum to 12 mm at 100 Pa pressure and finally 10 mm at 600 Pa pressure.

To further characterize the plasma plume, spatial distributions of W^{2+}, W^+ and WO^+ ion currents at 100 Pa background pressure were obtained with mass spectra also shown in Fig. 11. The

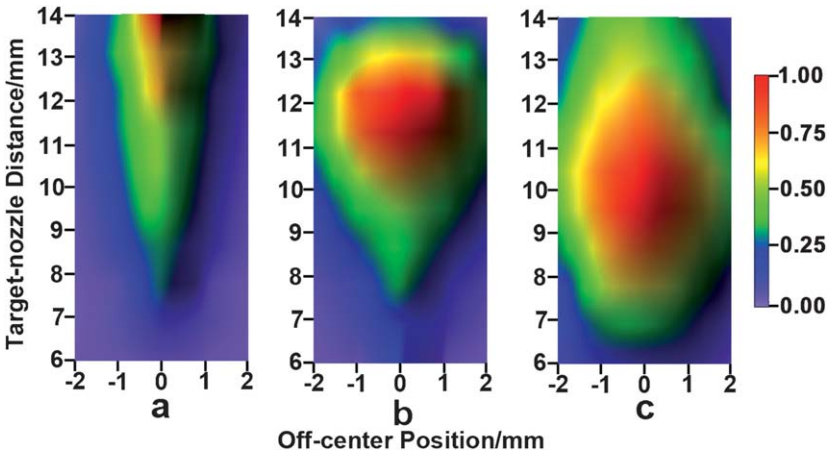

Fig. 10 Spatial distributions of W^+ (a) in vacuum, at (b) 100 Pa and (c) 600 Pa pressure of He. Parts (b) and (c) represent spatial distributions of the slow components in the ion packets with a deflect voltage of −4200 V and −4500 V, respectively.

formation of WO^+ is due to the residual oxygen in the buffer gas or ion source. The spectra in Fig. 11 show the highest intensities of the three species at the delay time of 18 μs for W^{2+}, 70 μs for W^+ and 80 μs for WO^+. If the TOF time for W^+ from the source to the repelling region is 70 μs, then, the TOF time for W^{2+} and WO^+ should be 49 μs and 73 μs, respectively, if all three species have the same kinetic energy. Thus, the kinetic energies of the three species are in the order of $W^{2+} > W^+ > WO^+$, which can also be verified through the deflect voltages at which the maximal intensities are reached (in the caption of Fig. 11).

As mentioned above, there is a coulomb acceleration effect in the direction of the target normal which is proportional to the charge state. As a consequence, the doubly charged ions are propelled to the sheath of the plume with the highest intensity locating at 14 mm or above. The interaction time with background gas atoms is very much reduced for W^{2+} due to its large energy acquisition during hydrodynamic acceleration. Thus, with respect to the singly charged ion emission, a high charge state leads to an increase in the directivity of the W^{2+} distribution around the target normal. This result is coincident with the work reported by Thum-Jaeger *et al.* that, in the vacuum condition, the maximal ejection of ions with highest charge state dominates in the direction of target normal and their concentration decreases sharply away from the nozzle axis.[32] It has also been

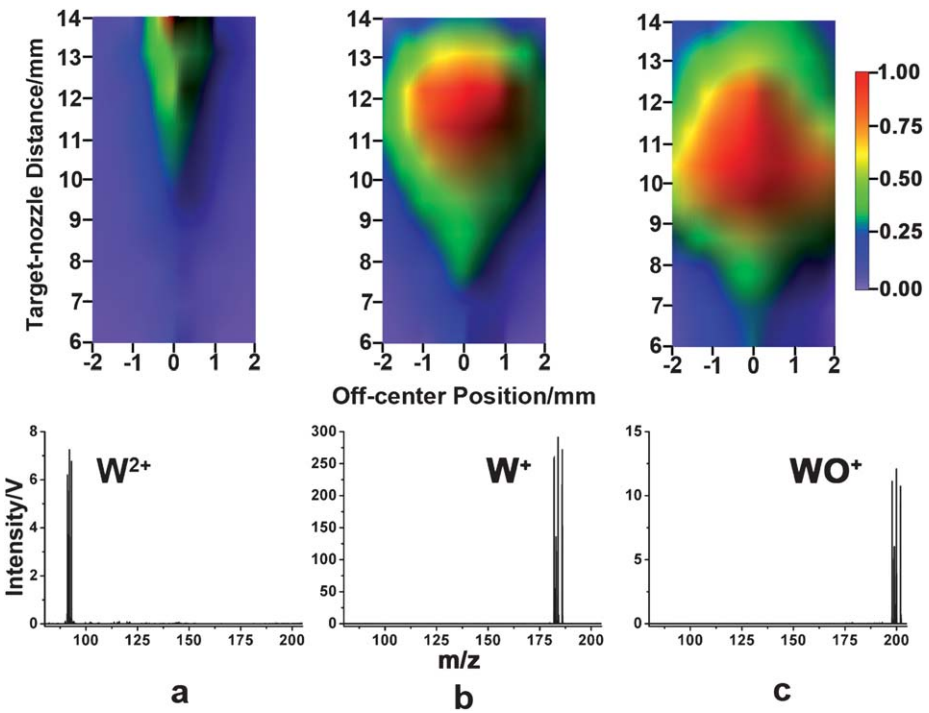

Fig. 11 Spatial distributions and mass spectra for the maximum intensities of (a) W^{2+} (acquired at the delay time of 18 μs, deflect voltage of −3200 V), (b) W^+ (delay time of 70 μs, deflect voltage of −4200 V), and (c) WO^+ (delay time of 80 μs, deflect voltage of −4500 V) at 100 Pa pressure of He. The intensities in the spatial distributions of W^{2+}, W^+, and WO^+ are normalized.

demonstrated that the aggregation processes of small species in the ablated plume are responsible for polyatomic ion formation, which results in polyatomic ions towards the tail of the plume.[7] Thus, WO^+ in the plume reaches its highest intensity at a distance of 10 mm from the target surface, which is shorter than that of W^+. The smaller kinetic energy for WO^+ could be caused by its larger collisional cross-section. This can be further confirmed through the delay time at which its maximal intensity is reached.

4. Conclusions

Characterization of laser ionization in vacuum and low pressure background gas was investigated by LI-*O*-TOFMS. The kinetic energy distributions of ionic species were measured by varying the deflect voltage and the delay time between the laser shot and the repelling pulse. A plume splitting was observed in the low pressure regime. It is characterized by a fast component at the vacuum velocity and a slow component which is affected by the background gas. The translation of plume dynamic was investigated from a free expansion in vacuum to shockwave-like expansion at relative low pressure and finally diffusion into background gas at relative high pressure. The topological graphs showing the spatial distributions of ions in the ion source were presented. A plume confinement was observed in the low pressure regime, which is more effective with the increase of the background gas pressure. Different expansion dynamics of W^{2+}, W^+ and WO^+ were also examined, which indicates that the kinetic energy is in the order of $W^{2+} > W^+ > WO^+$.

Acknowledgements

We gratefully acknowledge financial support from the Natural Science Foundation of China Financial (No. 20775063 and 21027011) and National 863 program (No. 2009AA06Z109). This work has also been supported by NFFTBS (No. J1030415).

References

1 D. H. Lowndes, D. B. Geohegan, A. A. Puretzky, D. P. Norton and C. M. Rouleau, *Science*, 1996, **273**, 898–903.
2 H. W. Kroto, J. R. Heath, S. C. O'Brien, R. F. Curl and R. E. Smalley, *Nature*, 1985, **318**, 162–163.
3 D. B. Geohegan, A. A. Puretzky, G. Duscher and S. J. Pennycook, *Appl. Phys. Lett.*, 1998, **72**, 2987–2989.
4 G. M. Hieftje, D. P. Myers, G. Q. Li, P. P. Mahoney, T. W. Burgoyne, S. J. Ray and J. P. Guzowski, *J. Anal. At. Spectrom.*, 1997, **12**, 287–292.
5 J. Pisonero and D. Gunther, *Mass Spectrom. Rev.*, 2008, **27**, 609–623.
6 D. Cleveland, P. Stchur, X. D. Hou, K. X. Yang, J. Zhou and R. G. Michel, *Appl. Spectrosc.*, 2005, **59**, 1427–1444.
7 Y. Lin, Q. Yu, W. Hang and B. Huang, *Spectrochim. Acta, Part B*, 2010, **65**, 871–883.
8 S. S. Harilal, B. O'Shay, Y. Z. Tao and M. S. Tillack, *J. Appl. Phys.*, 2006, **99**, 1–10.
9 S. S. Harilal, C. V. Bindhu, M. S. Tillack, F. Najmabadi and A. C. Gaeris, *J. Appl. Phys.*, 2003, **93**, 2380–2388.
10 S. S. Harilal, C. V. Bindhu, M. S. Tillack, F. Najmabadi and A. C. Gaeris, *J. Phys. D: Appl. Phys.*, 2002, **35**, 2935–2938.
11 S. Amoruso, R. Bruzzese, R. Velotta, N. Spinelli, A. Vitiello and X. Wang, *Appl. Surf. Sci.*, 2005, **248**, 45–49.
12 S. Amoruso, B. Toftmann, J. Schou, R. Velotta and X. Wang, *Thin Solid Films*, 2004, **453–454**, 562–572.
13 R. F. Wood, J. N. Leboeuf, K. R. Chen, D. B. Geohegan and A. A. Puretzky, *Appl. Surf. Sci.*, 1998, **127**, 151–158.
14 R. F. Wood, K. R. Chen, J. N. Leboeuf, A. A. Puretzky and D. B. Geohegan, *Phys. Rev. Lett.*, 1997, **79**, 1571–1574.
15 G. Mainfray and C. Manus, *Rep. Prog. Phys.*, 1975, **54**, 1333–1372.
16 G. Asimellis, A. Giannoudakos and M. Kompitsas, *Anal. Bioanal. Chem.*, 2006, **385**, 333–337.
17 J. Singh and S. Thakur, ed., *Laser-Induced Breakdown Spectroscopy*, American Elsevier Publishing Company, Inc., 2007.
18 S. Amoruso, R. Bruzzese, N. Spinelli and R. Velotta, *J. Phys. B: At., Mol. Opt. Phys.*, 1999, **32**, R131–R172.
19 B. Yan, L. F. Li, Q. A. Yu, W. Hang, J. He and B. L. Huang, *J. Am. Soc. Mass Spectrom.*, 2010, **21**, 1227–1234.
20 R. F. Huang, Y. M. Lin, L. F. Li, W. Hang, J. He and B. L. Huang, *Anal. Chem.*, 2010, **82**, 3077–3080.
21 Y. Lin, Q. Yu, R. Huang, W. Hang, J. He and B. Huang, *Spectrochim. Acta, Part B*, 2009, **64**, 1204–1211.
22 P. Ecija, M. N. S. Rayo, R. Martinez, B. Sierra, C. Redondo, F. J. Basterretxea and F. Castano, *Phys. Rev. A*, 2008, **77**, 1–8.
23 K. R. Chen, J. N. Leboeuf, R. F. Wood, D. B. Geohegan, J. M. Donato, C. L. Liu and A. A. Puretzky, *J. Vac. Sci. Technol., A*, 1996, **14**, 1111–1114.
24 N. M. Bulgakova, A. V. Bulgakov and O. F. Bobrenok, *Phys. Rev. E*, 2000, **62**, 5624–5635.
25 S. S. Harilal, *Appl. Surf. Sci.*, 2001, **172**, 103–109.
26 X. Y. Chen, S. B. Xiong, Z. S. Sha and Z. G. Liu, *Appl. Surf. Sci.*, 1997, **115**, 279–284.
27 J. Gonzalo, R. G. San Roman, J. Perriere, C. N. Afonso and R. P. Casero, *Appl. Phys. A: Mater. Sci. Process.*, 1998, **66**, 487–491.
28 S. Amoruso, B. Toftmann and J. Schou, *Appl. Phys. A: Mater. Sci. Process.*, 2004, **79**, 1311–1314.
29 R. F. Wood, J. N. Leboeuf, D. B. Geohegan, A. A. Puretzky and K. R. Chen, *Phys. Rev. B*, 1998, **58**, 1533–1543.
30 S. Amoruso, J. Schou and J. G. Lunney, *Europhys. Lett.*, 2006, **76**, 436–442.
31 R. W. Dreyfus, *J. Appl. Phys.*, 1991, **69**, 1721–1729.
32 A. Thum-Jaeger, B. K. Sinha and K. P. Rohr, *Phys. Rev. E*, 2001, **6302**, 1–10.
33 Y. Li, X. J. Yang, Y. X. Tang and Q. Z. Qin, *Appl. Spectrosc.*, 2000, **54**, 645–650.
34 M. I. Zeifman, B. J. Garrison and L. V. Zhigilei, *J. Appl. Phys.*, 2002, **92**, 2181–2193.
35 A. V. Gusarov, A. G. Gnedovets and I. Smurov, *J. Appl. Phys.*, 2000, **88**, 4352–4364.
36 A. V. Gusarov, A. G. Gnedovets and I. Smurov, *Appl. Surf. Sci.*, 2000, **154**, 66–72.

